sciendo

Polish Journal of Chemical Technology, 24, 3, 41—52, 10.2478/pjct-2022-0021

Effect of elevated pressure on gas-solid flow properties in a powder feeding system

Guanlong Ren[1, 2], Haijun Sun[1, 2, *], Yihua Xu[1, 2], Chao Li[3]

[1]*School of Aircraft Engineering, Nanchang Hangkong University, Nanchang 330063, China*
[2]*Jiangxi Key Laboratory of Micro Aero-engine, Nanchang 330063, China*
[3]*Unmanned System Research Institute, Northwestern Polytechnical University, Xi'an 710072, China.*
[*]*Corresponding author: e-mail: sunhaij1987@163.com*

In view of the powder feeding system, a multi-physical coupling model of the gas-powder-piston was established based on the Euler-Euler two-fluid model. The numerical simulation method was applied to explore the effects of dense gas-solid flow characteristics under different operating pressures. The results show that gas-solid pulsations at different operating pressures are mainly concentrated in the upper part of the powder tank. An elevated operating pressure efficiently decreases the powder layer area (ε_p = 0.1) fluctuation. As the operating pressure increases from 0.5 MPa to 3.0 MPa, the rising time and fluctuation rate of pressure are reduced by 71.4% and 62.3%, respectively, and the pressure in the tank has a long stabilization period. Meanwhile, the variation of the instantaneous powder flow rate is more stable and its average value is closer to the theoretical. A high-pressure environment is more conducive to the stable transportation of powder.

Keywords: Powder engine; Pressure effect; Dense gas-solid two-phase flow; Euler-Euler two-fluid model; Numerical simulation.

INTRODUCTION

With the continuous development of near-Earth and deep space exploration technology, a new concept powder engine that uses high-energy metal powder as fuel has gradually emerged[1, 2]. Due to the special characteristics of powder fuel, it can realize flexible regulation of fuel flow rate and make the engine with multi-pulse start-stop and thrust adjustment functions. In addition, by matching different types of fuels with oxidizers, or using a combination with conventional engines, a variety of powder engine types have been developed, such as powder-fueled ramjet engines[3, 4], Al/AP powder rocket engines[5] and Mg/CO_2 powder engines[6, 7], and powder--fueled water ramjet engines[8, 9].

The process of powder fluidization and conveying in the powder supply system can be achieved with the help of a corresponding carrier. Powder fluidization technology based on this property has been widely used in the chemical industry and other fields[10, 11], but it cannot be directly applied in powder supply systems. The reason is that the effect of powder fluidization on engine combustion performance needs to be considered. Therefore, how to better solve the application of powder fluidization technology in powder engines is still a key and difficult problem that needs to be solved urgently. In the early stages, Frick et al.[12] designed an industrial fluidized bed-type powder fuel supply device and conducted an experimental study on the conveying performance of the device. Based on this, Meyer et al[13] improved the powder fuel supply device by connecting the inlet pipe of fluidized gas to the piston end orifice to distribute the fluidized gas uniformly and prevent powder backflow. Due to the complexity of the powder supply system structure, Foote et al.[14] modified it to a Positive Displacement Fluidized Bed (PDFB) supply system, which can move the piston during the powder supply process more smoothly. With the continuous development of powder supply technology, Miller et al.[15] further improved the powder supply device by conveying the gas to the powder bed through a hose, which can better regulate the pressure in the powder storage tank.

The powder conveying process and fluidization characteristics are easily affected by the changes in operating pressure, piston velocity, and some properties of gases and powders themselves. In fact, there will be a gradual buildup of pressure in the powder storage tank when the powder engine is in firing condition. Hence, in order to ensure the powder fuel can be taken into the combustor, the pressure of the powder storage tank must be higher than that of the combustor, indicating the powder fuel transport process is under a high-pressure state. At this time, the fluidization process and the conveying process of powder under a high-pressure environment have greater uncertainty. Therefore, it's necessary to study the gas-solid two-phase flow characteristics under a high-pressure environment. Cai et al.[16] studied the flow characteristics of dense-phase pneumatic conveying under high pressure and analyzed the effects of fluidization number and particle size on the stability of the discharge. Song et al.[17] studied the effects of pressure increases on gas-solid fluidized beds, and the results showed that the increase in pressure can increase the minimum fluidization velocity of powder and change the bubble behavior. Liu et al.[18] studied the effects of pressure increase on the gas-solid flow behavior of a circulating fluidized bed, and the results showed that with the increase of operating pressure, the gas-solid slip velocity decreased and the powder volume fraction at the center of the lifting tube was larger. Shabanian et al.[19] explored the effect of pressure on the fluid dynamics of a gas-solid fluidized bed and believed that an increase in operating pressure could either increase the degree of charge in the bed by accelerating gas adsorption. Sun et al.[20, 21] carried out experimental and numerical research on powder fluidization characteristics under high-pressure environments and further studied the pneumatic starting characteristics of powder fuel under high-pressure environments. The results show that under a high-pressure environment, the powder can form

a stable gas-solid interface, which provides a reference for the stable delivery of the powder.

There is an extremely complex powder fluidization transport process that exists in piston-driving powder supply devices under high-pressure environments, involving the mutual coupling effect of gas-powder-piston. Although there have been many relevant experimental reports[22, 23], they are greatly restrictive in revealing the details of gas-solid flow and the interaction mechanism. The present work, based on relevant experiments and numerical simulation methods, is dedicated to investigating the effects of different initial operating pressure environments on the flow behavior of dense gas-solid two-phase flows (e.g. the powder fluidization process, the spatial distribution of the powder layer, the variation in powder velocity, the pressure in the powder storage tank, and the variation of the powder mass flow rate). It has significant practical meaning for the optimal design of the powder fuel supply system.

GEOMETRIC MODELS AND NUMERICAL SIMULATION SETUP

Powder storage tank geometry model

Figure 1 shows the configuration and dimensions of the powder storage tank. The powder storage tank in the figure is placed horizontally and is mainly composed of three parts: the cylinder section, the convergence section, and the horizontal pipeline. The cylinder section has a diameter of 60 mm and a length of 150 mm. The convergence section is connected to the front end of the cylinder section with a 45° convergence angle and a 27 mm length, in which an annular slit intake with a width of 1.41 mm is arranged at the center position of the convergence section. The horizontal pipeline is connected to the front end of the convergence section with a 17 mm length. A two-phase nozzle with a throat diameter of 3 mm is arranged at the horizontal pipeline to prevent the gravity settlement of powder. Besides, the piston is simplified as a moving wall in this study, which is installed at the rear end of the cylinder section. The detailed parameters are shown in Figure 1.

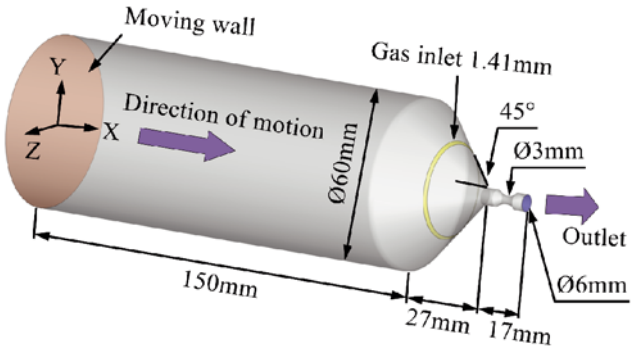

Figure 1. Powder storage tank configuration

Two-Fluid Model

Governing equations of two-fluid model

The two-fluid model (TFM) regards the continuous and discrete phases in space as a continuous medium that can permeate each other, and this method is also called the Euler-Euler method[24–27]. They are described in the Eulerian coordinate system using the mass, momentum, and energy conservation equations for the macroscopic continuum fluid. The detailed governing equations are presented in Table 1.

Table 1. Two-fluid model equations

Continuous equations:	
Gas phase	
$\frac{\partial(\varepsilon_g\rho_g)}{\partial t}+\nabla(\varepsilon_g\rho_g\mathbf{u}_g)=0$	(1)
Solid phase	
$\frac{\partial(\varepsilon_s\rho_s)}{\partial t}+\nabla(\varepsilon_s\rho_s\mathbf{u}_s)=0$	(2)
$\varepsilon_g+\varepsilon_s=1$	(3)
Momentum equations:	
Gas phase	
$\varepsilon_g\rho_g(\frac{\partial\mathbf{u}_g}{\partial t}+\mathbf{u}_g\nabla\mathbf{u}_g)=-\varepsilon_g\nabla p+\nabla\cdot\tau_g+\beta(\mathbf{u}_p-\mathbf{u}_g)+\varepsilon_g\rho_g\mathbf{g}$	(4)
$\tau_g=\varepsilon_g\mu_g(\nabla\mathbf{u}_g+(\nabla\mathbf{u}_g)^T)+\varepsilon_g(\lambda_g-\frac{2}{3}\mu_g)\nabla\cdot\mathbf{u}_g\mathbf{I}$	(5)
Solid phase	
$\varepsilon_s\rho_s(\frac{\partial\mathbf{u}_s}{\partial t}+\mathbf{u}_s\nabla\mathbf{u}_s)=-\varepsilon_s\nabla p-\nabla p_s+\nabla\cdot\tau_s+\beta(\mathbf{u}_g-\mathbf{u}_s)+\varepsilon_s\rho_s\mathbf{g}$	(6)
$\tau_s=\varepsilon_s\mu_s(\nabla\mathbf{u}_s+(\nabla\mathbf{u}_s)^T)+\varepsilon_s(\lambda_s-\frac{2}{3}\mu_s)\nabla\cdot\mathbf{u}_s\mathbf{I}$	(7)

Kinetic theory of granular flow

Much of the research on gas-solid two-phase flow has employed the kinetic theory of granular flow (KTGF), which was established in recent years, to close the solid phase force[25]. The theoretical idea originates from molecular kinetic theory[28], which has been widely applied, and the related model derivation can be referred to relevant studies[29–31]. The primary model equations are expressed in Table 2.

Interphase interaction

The drag force is the most important parameter, which is usually used to describe the gas-solid interphase interaction. And its magnitude is affected by many factors, including the shape of the particles and the form of their existence[32–34]. Therefore, it is necessary to choose an appropriate drag force model to make the model prediction more accurate. The classical Gidaspow model[29] is selected to describe the gas-solid interphase interaction. The detailed equations are presented in Table 3.

Numerical simulations

The TFM and KTGF are chosen for the simulation of the dense gas-solid two-phase flow and the closure of the solid phase in the conservation equation[25] respectively. The RNG k-ε turbulence model and the PC-SIMPLE (Phase Coupled SIMPLE) algorithm are used for the description of the gas phase and solve the pressure-velocity coupled problem respectively. The second-order upwind scheme is applied to all other governing equations. A transient pressure-based solver is chosen to track flow rate changes over time with a time step of 0.0005 s.

The initial powder bed in the range of X-axial [0, 0.177 m], Y-axial [–0.03 m, 0.03 m], and Z-axial [–0.03 m, 0.03 m] is used in all simulation cases. Mass flow rate and pressure boundary conditions are applied to the gas inlet and two-phase outlet respectively. The wall is defined with a no-slip boundary condition, and piston motion is achieved by using a User Defined Function (UDF) code. Air and aluminum are used as the fluidized

Table 2. KTGF model equations

Solid pressure:

$$p_s = \varepsilon_s \rho_s \Theta_s + 2\rho_s \Theta_s (1+e)\varepsilon_s^2 g_0 \tag{8}$$

Solid shear stresses:

$$\mu_s = \mu_{s,col} + \mu_{s,kin} + \mu_{s,fr} \tag{9}$$

Solid collision viscosity:

$$\mu_{s,col} = \frac{4}{5}\varepsilon_s \rho_s d_s g\ (1_0 + e)\left(\frac{\Theta_s}{\pi}\right)^{1/2} \tag{10}$$

Kinetic viscosity:

$$\mu_{s,kin} = \frac{10 d_s \rho_s \sqrt{\Theta_s \pi}}{96(1+e)g_0}\left[1 + \frac{4}{5} g_0\, \varepsilon_s (1+e)\right]^2 \tag{11}$$

Frictional viscosity:

$$\mu_{s,fr} = \frac{P_s \sin\phi}{2\sqrt{I_{2D}}} \tag{12}$$

Gas and solid phases bulk viscosity:

$$\lambda_g = 0, \lambda_s = \frac{4}{3}\varepsilon_s \rho_s d_s g_0 (1+e)\left(\frac{\Theta_s}{\pi}\right)^{1/2} \tag{13}$$

Diffusion coefficient of granular energy:

$$\Gamma_{\Theta_s} = \frac{150 \rho_s d_s \sqrt{\Theta_s \pi}}{384(1+e)g_0}\left[1 + \frac{6}{5}\varepsilon_s g_0 (1+e)\right]^2 + 2\rho_s \varepsilon_s^2 d_s (1+e) g_0 \left(\frac{\Theta_s}{\pi}\right)^{1/2} \tag{14}$$

Collision energy dissipation:

$$\gamma_{\Theta_s} = \frac{12(1-e^2)g_0}{d_s\sqrt{\pi}} \rho_s \varepsilon_s^2 \Theta_s^{3/2} \tag{15}$$

Radial distribution function:

$$g_0 = \left[1 - \left(\frac{\varepsilon_s}{\varepsilon_{s,\max}}\right)^{1/3}\right]^{-1} \tag{16}$$

Granular energy equation:

$$\Theta_s = \frac{1}{3}\overline{u_{s,i}^2} \tag{17}$$

$$\frac{3}{2}\left[\frac{\partial}{\partial t}(\rho_s \alpha_s \Theta_s) + \nabla \cdot (\rho_s \alpha_s \mathbf{u}_s \Theta_s)\right] = (-p_s \mathbf{I} + \tau_s) : \nabla \mathbf{u}_s + \nabla \cdot (k_{\Theta_s} \nabla \Theta_s) - \gamma_{\Theta_s} - 3\beta\Theta_s \tag{18}$$

Table 3. Gidaspow model equations

$$\beta = \begin{cases} \frac{3}{4}\frac{(1-\varepsilon_g)\varepsilon_g}{d_s}\rho_g\left|\mathbf{u}_g-\mathbf{u}_s\right|C_d\varepsilon_g^{-2.65} & \varepsilon_g > 0.8 \\ 150\frac{(1-\varepsilon_g)^2\mu_g}{\varepsilon_g d_s^2}+1.75\frac{(1-\varepsilon_g)\rho_g\left|\mathbf{u}_g-\mathbf{u}_s\right|}{d_s} & \varepsilon_g \le 0.8 \end{cases} \quad (19)$$

$$C_d = \begin{cases} \frac{24}{Re_s}(1+0.15Re_s^{0.687}) & Re_s < 1000 \\ 0.44 & Re_s \ge 1000 \end{cases} \quad (20)$$

$$Re_s = \frac{\varepsilon_g\rho_g\left|\mathbf{u}_g-\mathbf{u}_s\right|d_s}{\mu_g} \quad (21)$$

gas and powder fuel, and the gas intake mass flow rate is given as a percentage of the theoretical value obtained by piston velocity back-calculation. The equation is presented below.

$$\dot{m}_{pt} = \rho_{packing} v_{piston} A_{piston} = \rho_p \varepsilon v_{piston} A_{piston} \quad (22)$$

where $\dot{m}_{pt}$ is the theoretical powder mass flow rate, $\varrho_{packing}$ is the initial powder packing density, v_{piston} is the piston (moving wall) velocity, A_{piston} is the piston (moving wall) area, ϱ_p is the powder density, and ε is the initial powder packing volume fraction.

The different numerical simulation cases and specific operating conditions are shown in Tables 4 and 5.

Grid independency

The ICEM software is employed to generate structured hexahedral meshes of the powder storage tank, and the meshing results are shown in Figure 2. To verify the grid independence, four grids with 0.10, 0.35, 0.60, and 0.80 million cells each are employed. Figure 3 shows the effects of four different grid cells on the axial velocity and volume fraction of the powder at X = 0.140 m. It can be seen that there is a small overall difference between 0.35, 0.60, and 0.80 million cells, while 0.10 million cells have a large difference compared with other grids. As a result, the grid consisting of 0.35 million cells is chosen to shorten the calculation time.

Table 4. Case relevance with parameter testing

Case	Operating pressures (MPa)	Piston velocity (m/s)
1	0.5	0.07
2	1.0	0.07
3	1.5	0.07
4	2.0	0.07
5	2.5	0.07
6	3.0	0.07

Table 5. Operation conditions

Parameters	Value
Intake gas mass flow rate (kg/s)	0.0025
Average powder diameter (mm)	0.02
Initial powder packing volume fraction	0.55
Maximum powder packing volume fraction	0.63
Gravitational acceleration (m/s^2)	9.81
Powder viscosity (pa·s)	1.72e^{-5}
Powder density (kg/m^3)	2719
Dummy mass coefficient	0.5
Restitution coefficient	0.9
convergence criteria	10^{-4}

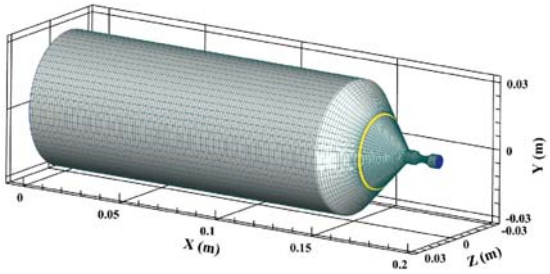

Figure 2. Structured hexahedral meshes of the powder storage tank

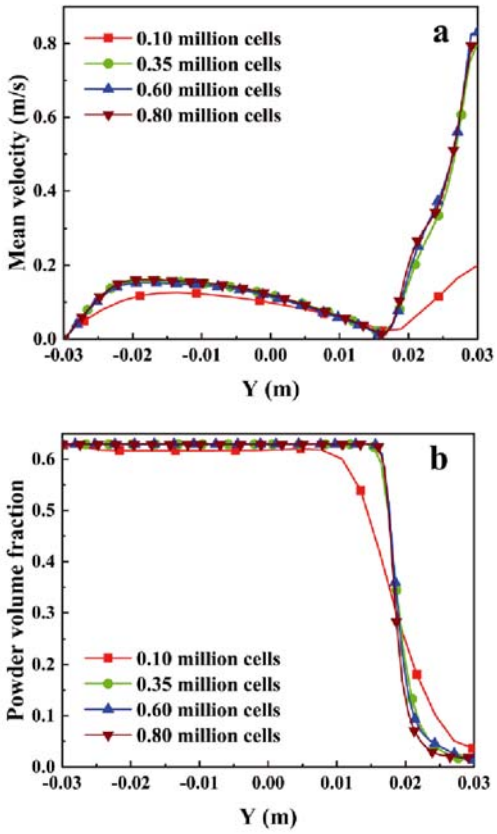

Figure 3. Grid independency test: (a) Mean powder axial velocity; (b) Powder volume fraction

RESULTS AND DISCUSSION

Verification of numerical model

To verify the accuracy of the numerical models used in this study, the results of the current numerical simulation data are compared with experiments[20]. The experimental apparatus used in Ref.[20] is mainly composed of a gas cylinder, a powder chamber, a pneumatic ball valve, a control computer, and a powder collector. Before the experiment, put the pre-weighted powder into the powder chamber, and then fill it with fluidized gas till it reaches a certain pressure. After that, open the pneumatic ball valve. The gas-solid flow will cause a pressure drop in the powder chamber, so the pressure drop at a certain experiment time is chosen as the parameter for numerical model verification. That is called the pressure drop rate. The pressure drop rate is defined as the difference between the initial fluidized pressure and the pressure at a stable stage within a fixed time interval, and the expression is as follows:

$$\Delta p = \frac{p_1 - p_0}{\Delta t} \tag{23}$$

where P_0 is the initial total pressure/MPa, P_1 is the pressure at the end/MPa, Δt is the time interval.

The relative errors (*ERR*) equation is expressed by the following Eq. (24):

$$ERR = \frac{|p_s - p_e|}{p_s} \tag{24}$$

where P_s is the numerical simulation data, P_e is the experimental data.

Table 6 gives the comparison of numerical simulation and experimental data. It can be seen that the relative error of Test 1 is greater than 12%, while other tests fluctuate below 12%. But, in general, the simulation results are in good agreement with the experiments, which meet the calculation requirements. The data comparison results show that the two-fluid model can be used efficiently to study the effects of different operating pressures on the fluidization and conveying characteristics of powders.

Powder fluidization process

Figure 4 shows the powder concentration distribution on the central section (Z = 0 m) of the powder storage tank at different moments. At t = 0.01 s (see Fig. 4(a)), the gas and powder phases under different cases show a symmetrical distribution. The gas exists in the form of bubbles in the powder bed in the convergence section, and its distribution size increases with the increase in operating pressure. At this time, the powders are picked up and transported out of the tank under the entrainment action of fluidized gas. At t = 0.10 s (see Fig. 4(b)), the symmetrical distribution phenomenon of gas and solid phases disappears. There is a phenomenon now that the gas cavity range in the upper part of the powder storage tank is larger than the lower. Meanwhile, the bubble size in the upper part of the powder storage tank decreases with increasing operating pressure. In Case 1, the powder is lifted near X = 0.160 m and the gas-solid interface is significantly disturbed, while the phenomenon gradually disappears with the increase of operating pressure. On the one hand, the explanation is that the decreasing operating pressure causes an increase in the gas velocity, which results in the effect of the entrainment and interference on the solid phase being obvious. On the other hand, the gas phase interacts with the solid phase and the wall to form a reflux vortex, which rolls up the powder, resulting in the powder being lifted up, which is not conducive to the formation of a stable gas-solid interface.

As shown in Figure 4(c) at t = 0.30 s, the bubbles for all cases in the upper part of the convergence section further expand toward the moving wall, and the bubble range decreases with the increase of operating pressure. Although the bubble distribution range in the lower part of the convergence section is small, the stability of the formed gas-solid interface is higher than in the upper part. This phenomenon can be explained by the fact that the powder will be deposited near the bottom of the cylinder and convergence section under the combined action of the piston thrust and powder gravity. The gas phase action zone in the lower part of the convergence section is squeezed, while the upper part leaves a large cavity. At this time, the gas phase effect in the lower part of the convergence section is weaker than the powder self-weight, resulting in the gas phase area being reduced. However, it will form a relatively stable gas-solid interface when the gas force and the powder self-weight make a dynamic balance. In addition, it can also be seen that the powder low concentration area in all cases appears in the upper part of the cylinder section, and its distribution area decreases with increasing operating pressure. On the one hand, the gas phase velocity and operating pressure are inversely proportional. When the operating pressure is low and the initial gas kinetic energy is high, the ability of entrainment and pick up on the powder is enhanced, the momentum transfer between the gas and the solid phases increases, and the movement of the powder is highly susceptible to the effect of the gas. On the other hand, when the amount of powder pushed by the moving wall is less than the powder output, the void is not filled in time and the powder low concentration area will also appear.

At t = 0.80 s (see Fig. 4(d)), the gas phase in different cases expands further and almost fills the upper part of the powder storage tank. And the range of the gas cavity shrinks with the increase in operating pressure. In

Table 6. Numerical model validation

Tests	1	2	3	4	5	6
Initial total pressure, (MPa)	0.5	1.0	2.0	3.0	4.0	5.0
Numerical simulation data, P_s (MPa/s)	0.37	0.74	1.51	2.42	3.34	4.26
Experimental data[20], P_e (MPa/s)	0.29	0.66	1.35	2.16	2.95	3.76
Relative error, *ERR* (%)	21.6	10.8	10.6	10.7	11.7	11.7

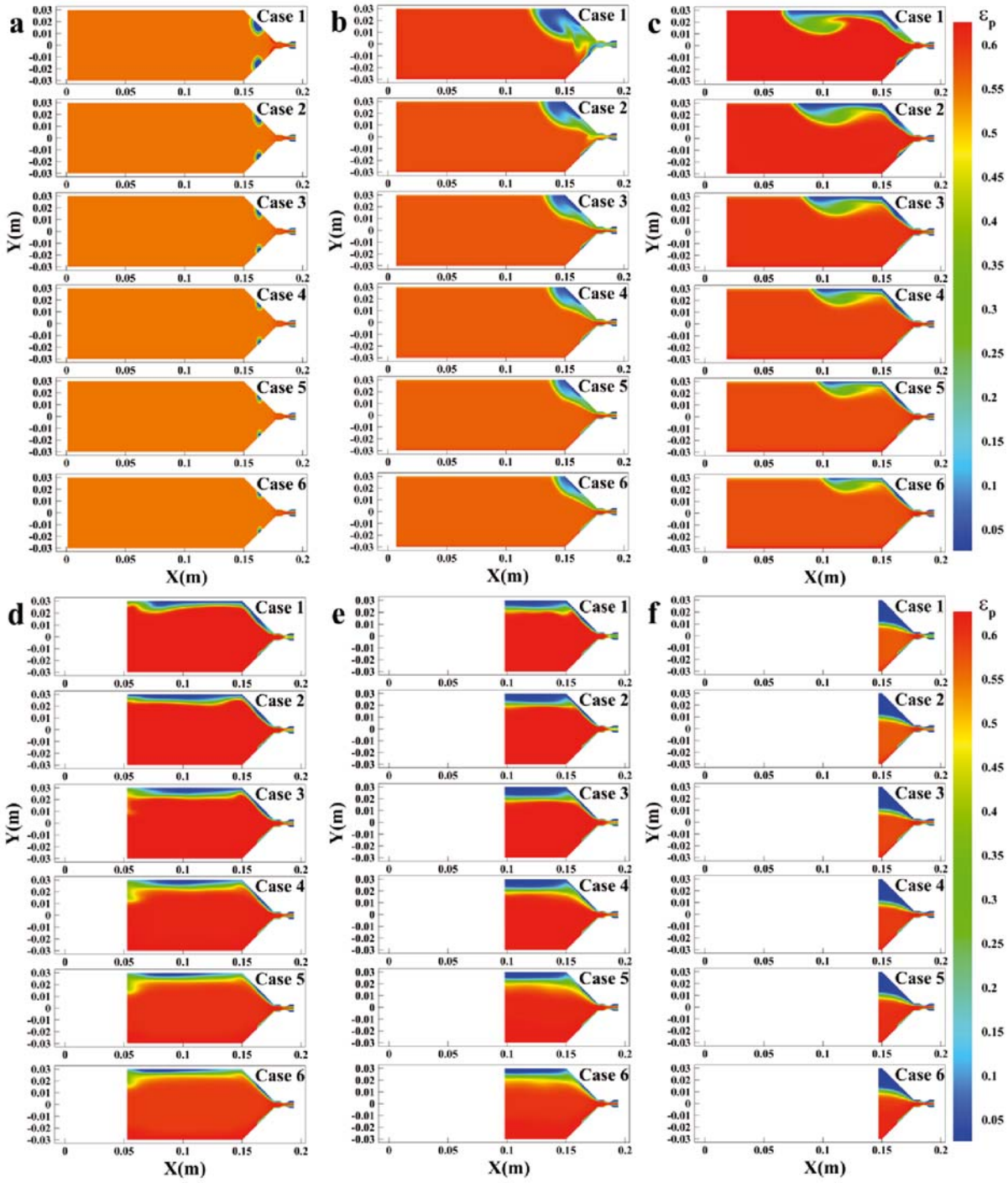

Figure 4. Powder fluidization process on the central section (Z = 0 m): (a) t = 0.01 s; (b) t = 0.10 s; (c) t = 0.30 s; (d) t = 0.80 s; (e) t = 1.40 s; (f) t = 2.10 s

addition, a region of lower powder concentration appears near the moving wall at higher operating pressure conditions, which is most obvious in Cases 4–6. The reason is that the amount of powder pushed by the piston and the amount of powder output by the gas entrainment do not reach a good match relationship, resulting in the occurrence of the phenomenon of powder shortage. At t = 1.40 s (see Fig. 4(e)) and t = 2.10 s (see Fig. 4(f)), the fluidization process tends to stabilize, and the gas phase has filled the upper part of the powder storage tank, where there is an obvious distribution boundary with the solid phase. At this time, there is a horizontal distribution of the gas-solid interface, indicating that the amount of powder pushed forward by the moving wall and powder output maintain dynamic balance. Furthermore, it can be seen that the powder bed height at the higher initial operating pressure is also relatively high, which is consistent with the results obtained in reference[35].

Distribution of the powder layer

From the analysis in the previous section, it is known that a relatively stable gas-solid interface or powder layer structure can be formed during the powder fluidization process and is accompanied by the appearance of a powder stratification phenomenon. In order to study the influence of different operating pressures on the spatial distribution of powder layers, the powder concentration ε_p = 0.1 is defined as the powder layer and its spatial distribution as shown in Figure 5. As shown, at t = 0.01 s (see Fig. 5(a)), the annular powder layer formed in all cases is distributed close to the convergence section wall, and its distribution range decreases

with the increase of operating pressure. At t = 0.10 s (see Fig. 5(b)), the annular powder layer disappears and gradually extends to the tail of the powder storage tank, and the extension region decreases with the increase of operating pressure. In addition, the maximum and minimum distribution of the powder layer correspond to Case 1 and Case 6 respectively in the radial range, indicating that the distribution of the powder is more influenced by the initial operating pressure. The reason is that the high-pressure environment effectively inhibits the bubble coalescence[35] and makes the entrainment ability of the gas to powder weaken. At t = 0.30 s (see Fig. 5(c)), the powder layer continues to extend towards the tank's end, and the extension speed and range decrease as the operating pressure increases. Besides, there is a downward concave phenomenon in the powder layer in the horizontal direction, and the degree of depression is smaller at higher initial operating pressure. Combined with the powder fluidization process in Figure 4, the main reason is that the powder output volume and the filling volume did not reach the precise matching relationship, which leads to variations in powder concentration and makes the powder layer unevenly distributed.

At t = 0.80 s (see Figure 5(d)), the downward concave phenomenon of the powder layer in Cases 2–6 disappears, indicating that the gas cavity is filled in time by the powder pushed forward by the piston. For Case 1, only a small change in the powder layer occurs, which is mainly attributed to the perturbation effect of the gas. What's more, the powder layer distribution shrinks along the radial direction at X = 0.150 m as the operating pressure increases. Combined with the powder fluidization process in Figure 4, it shows that the height of the powder bed is proportional to the operating pressure, which is especially obvious in Case 6. At t = 1.40 s (see Fig. 5(e)) and t = 2.10 s (see Fig. 5(f)), the distribution of powder layers is smooth, which is hardly affected by the variation of initial operating pressure. The main reason is that, in the fluidization stable stage, the powder is in a compacted state under gravity and the push of moving walls, and the gas kinetic energy cannot resist the combined effect of gravity and drag force, which greatly reduces the perturbation capacity of the gas on the powder. Overall speaking, in the start-up stage, the processes of bubble breakup and coalescence as well as the pushing effect of the moving wall have a great influence on the powder distribution, while the influence is greatly reduced in the stable stage.

For quantitative analysis of the change process of the above powder layer, the standard deviation is chosen to describe the fluctuation degree of the powder layer area, and the expressions are as follows:

$$STD = \sqrt{D(\dot{A})} = \sqrt{\frac{1}{N}\sum_{i=1}^{N}(\dot{A}_i - \mu_{\dot{A}})^2} \tag{25}$$

$$\mu_{\dot{A}} = \frac{1}{N}\sum_{i=1}^{N}\dot{A}_i, i = 1,2,3\cdots,N \tag{26}$$

$$D(\dot{A}) = E\left\{\left[\dot{A}(t) - \mu_{\dot{A}}\right]^2\right\} = \frac{1}{N}\sum_{i=1}^{N}(\dot{A}_i - \mu_{\dot{A}})^2 \tag{27}$$

where $\mu_{\dot{A}}$ is the mathematical expectation of the powder layer area, $D(\dot{A})$ is the variance of the powder layer area.

The variation law of the powder layer area for all cases with time is given, as shown in Figure 6. It can be seen that the variation of powder layer area under different operating pressures can be divided into the rising stage and the falling stage. In the rising stage, there is a small area peak in all cases, and the value decreases with increasing operating pressure, which is due to the gas having a strong impact on the powder in the start-up stage, resulting in changes to the powder layer area. Immediately afterwards, the area reaches a maximum, whose value decreases with the increase of operating pressure, and the corresponding moment advances with increasing operating pressure. In particular, an obvious peak phenomenon appears in Case 1, and the value is about 58 cm^2. In the falling stage, an interesting phenomenon can be found: except for Case 1, the powder layer area decreases with increasing operating pressure for other cases, which is due to the gas in Case 1 causing greater entrainment effect on the powder in the

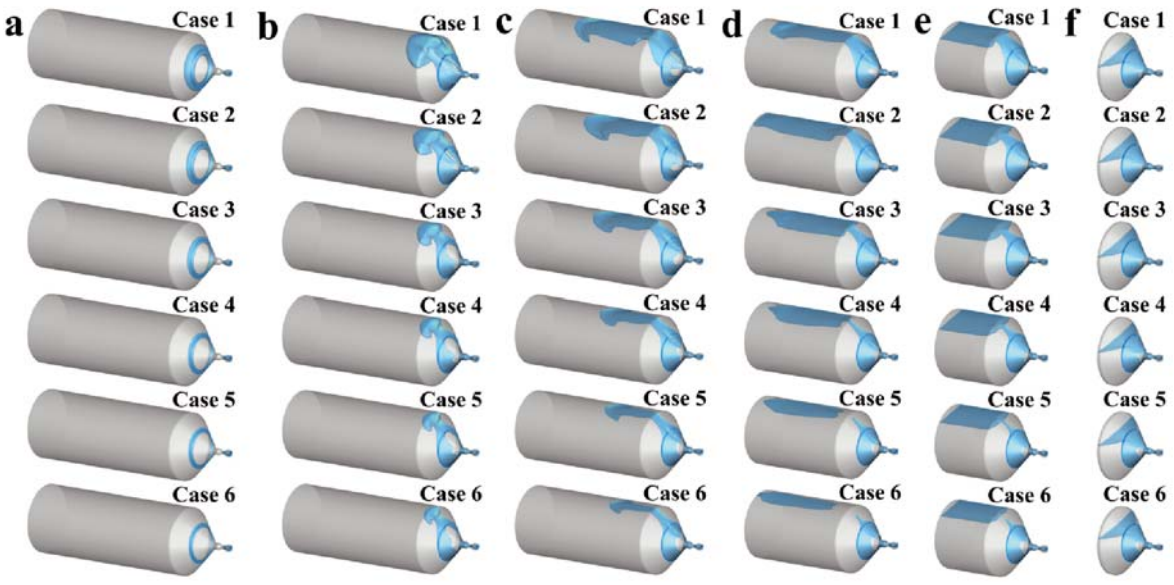

Figure 5. Spatial distribution of powder layers with different concentrations: (a) t = 0.01 s; (b) t = 0.10 s; (c) t = 0.30 s; (d) t = 0.80 s; (e) t = 1.40 s; (f) t = 2.10 s

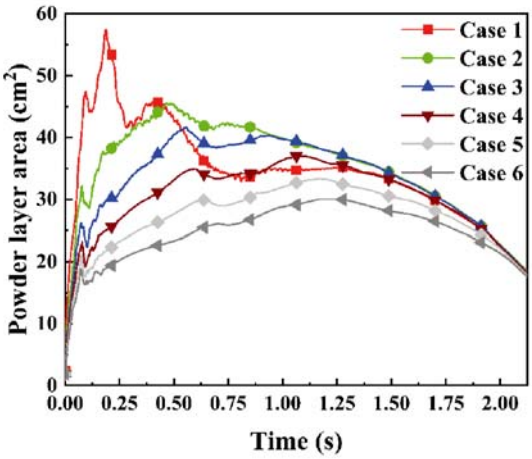

Figure 6. Variation of powder layer area with time under different cases

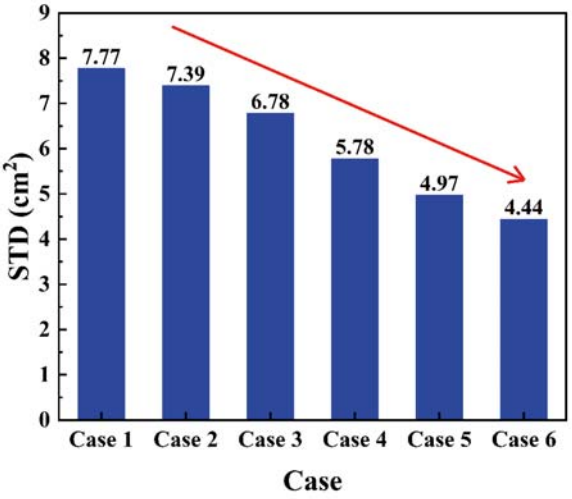

Figure 7. The standard deviation distribution of powder layer area

upper part of the tank, resulting in a disordered curve distribution.

Figure 7 shows the standard deviation distribution of the instantaneous powder layer area. It can be seen that the maximum and minimum values of the standard deviation correspond to Case 1 and Case 6, respectively, and their values have decreased by about 42.9%, indicating the powder layer area fluctuation decreases greatly with the increase of operating pressure. The reason is that the pressure mainly affects the gas density. When the gas phase density increases, it will correspondingly increase the powder motion drag and reduce the collision frequency between powders, thus making it more difficult for the powder to aggregate and a relatively uniform flow structure to be formed[35, 36]. Combined with the spatial distribution of the powder layer, the variation of instantaneous area, and the standard deviation distribution, it shows that the powder motion behavior is less affected by gas perturbation under high operating pressure conditions.

Powder velocity characteristics

Figure 8 shows the mean axial velocity of powder under all cases at X = 0.150 m on the central section (Z = 0 m). It can be seen that there is a significant difference in the powder velocity distribution at t = 0.10 s compared with other moments. As shown in Figure 8(a), at t = 0.10 s, the average velocity distribution of the powder under different cases is similar in the middle and lower parts of the powder storage tank, all linearly increasing to about 0.09 m/s. However, the distance of linear increase is different. For Case 1, the cutoff position for the linear increase is at 0.007 m on the Y-axial, while the cutoff position in Case 6 is at 0.018 m on the Y-axial. It can be seen that the range of linear increase along

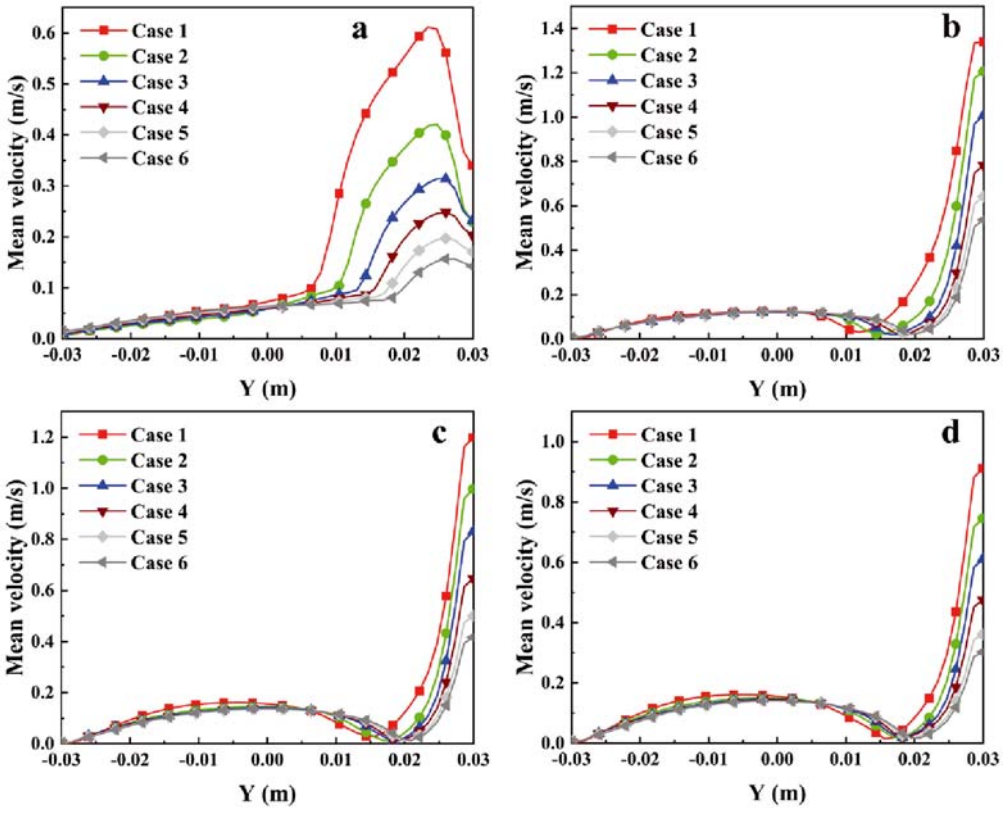

Figure 8. Mean axial velocity distribution of powder at different moments: (a) t = 0.10 s; (b) t = 0.80 s; (c) t = 1.40 s; (d) t = 2.10 s

the positive direction of Y-axial is larger with the increase of operating pressure. At this moment, the powder motion in this region is mainly influenced by the piston push. Subsequently, the powder velocity under different cases will show a sharp increase, accompanied by the appearance of velocity peaks, and the value decreases with the increase of operating pressure. When the initial operating pressure is high, the rising inflection point of velocity and the position of the Y-axial corresponding to the peak is closer to the upper part of the powder storage tank. Combined with the powder fluidization process (see Fig. 4), it can be explained that the violent motion behavior of the gas phase in this range leads to a large variation in the powder velocity.

At t = 0.80 s, as shown in Figure 8(b), the mean powder velocity distribution changed significantly, but the overall value increases slightly. In the range of Y-axial -0.030 m to 0.010 m, the velocity distribution of different cases remains consistent, first slowly increasing to 0.1 m/s and then slowly decreasing. In the range of Y-axial 0.010 m to 0.030 m, the powder velocity in Case 1 increases sharply, while in other cases it decreases continuously and then increases sharply. It can be explained that the entrainment effect of gas on powder in the upper wall of the tank and the momentum transfer between gas and solid phases are greatly enhanced, resulting in the powder velocity rising. Due to the gas in Case 1 having a higher initial velocity, the powder velocity is greater than the rest of the cases. Compared with the prior moment, the maximum powder velocity increased by about 1.3 times. At t = 1.40 s (see Fig. 8(c)) and t = 2.10 s (see Fig. 8(d)), the mean powder velocity distribution is similar to that of Figure 8(b), but the values differ slightly. On the one hand, the disturbance effect of the gas on the powder in the compacted state is changed due to the reduction of the powder amount in the tank. On the other hand, the increasing pressure in the powder storage tank reduces the entrain kinetic energy of the gas, resulting in the momentum exchange ability between gas and solid phases being weakened.

Pressure characteristics

The spatial locations X = 0.151 m, Y = 0.028 m, and Z = 0 m are chosen as the monitoring points for pressure in the powder storage tank. Figure 9 illustrates the distribution of the pressure-time curve measured at the monitoring point in different cases. As can be seen, the pressure changes in different cases can be divided into three main stages: the rising stage, the stable stage, and the falling stage. In the rising stage, the pressure rising ratios of Cases 1–6 are 3.14, 1.36, 0.82, 0.57, 0.41, and 0.32, respectively, indicating the pressure rising amplitude is smaller at higher operating pressure. As the operating pressure increases from 0.5 MPa to 3.0 MPa, the pressure rise time is shortened by 71.4%, thus allowing the pressure stability period to be extended. In the falling stage, the moving wall moves to near the position of the convergence section, which means the process of powder fluidization conveying is coming to an end. Meanwhile, the falling inflection point of each case is similar, while the decline rate reduces with the increase in operating pressure. The overall distribution trend of the pressure curve can be mainly explained by

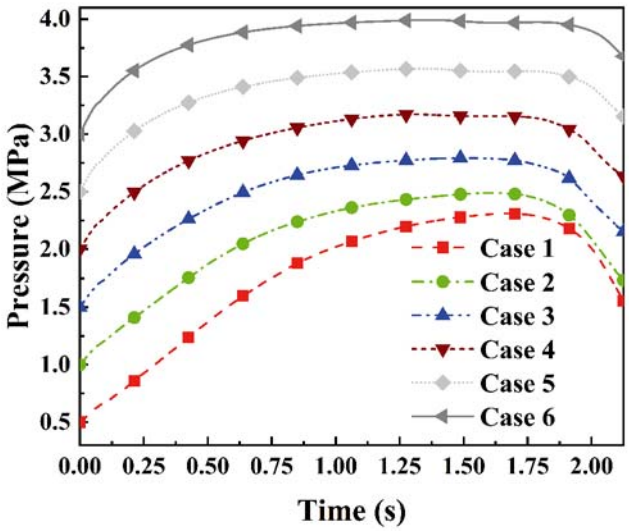

Figure 9. Pressure distribution in powder storage tank under different cases

the game relationship between gas inflow and outflow. Combined with the powder fluidization process (see Fig. (4)), it can be seen that the convergence section is almost filled with powder in the initial stage of fluidization. At this time, the gas is forced to flow inside of the powder storage tank, only a small amount out of the powder storage tank, resulting in the inflow being greater than the outflow and the pressure in the powder storage tank increasing. Besides, because the gas density at low pressure is lower, the gas cavity formed is larger, which makes the pressure in the powder storage tank rise faster. When the process of powder fluidization conveying is coming to an end, there is a large gas cavity in the upper part of the powder storage tank, which means the gas phase channel is enlarged in the horizontal pipeline. At this time, the contribution made by the gas in the gas--solid two-phase flow is greater, and the gas outflow is greater than the inflow, resulting in the pressure in the powder storage tank decreasing. In general, the game relationship between gas inflow and outflow under high--pressure environments is weaker, resulting in smaller pressure changes and long periods of stability.

Figure 10 presents the standard deviation distribution of the pressure under different cases. It can be seen that the standard deviation from Case 1 to Case 6 decreases significantly, and its value is reduced by about 62.3%. In other words, the pressure fluctuation decreases significantly as operating pressure increases. As for a piston-driving powder fuel supply system, by elevating the operating pressure, a more uniform gas-solid flow structure can be achieved and a more stable powder fluidization process can be maintained.

Mass flow rate characteristics of powder

For the powder feeding system, the output characteristics of the powder mass flow rate should be focused on. Figure 11 shows the instantaneous powder mass flow rate distribution for all cases. The phenomenon that the flow rate fluctuates with time is consistent with the results of powder fluidization visualization[20] and flow rate measurement[21].It can be seen that the powder mass flow rate in all cases shows a similar distribution law, which can be divided into two stages: the rising stage and the

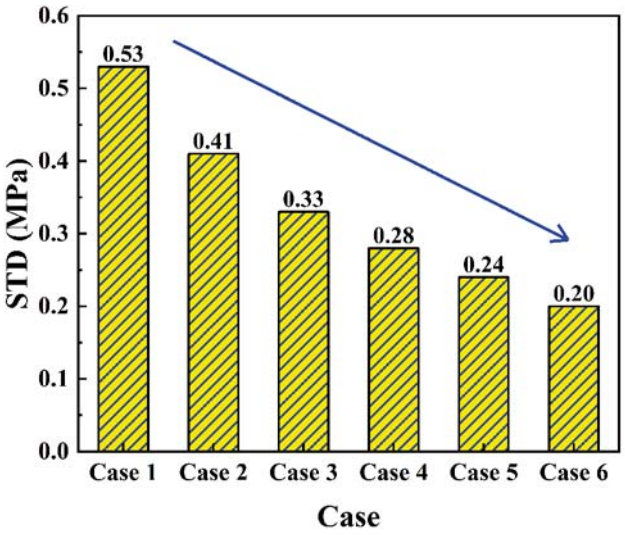

Figure 10. The standard deviation distribution of pressure under different cases

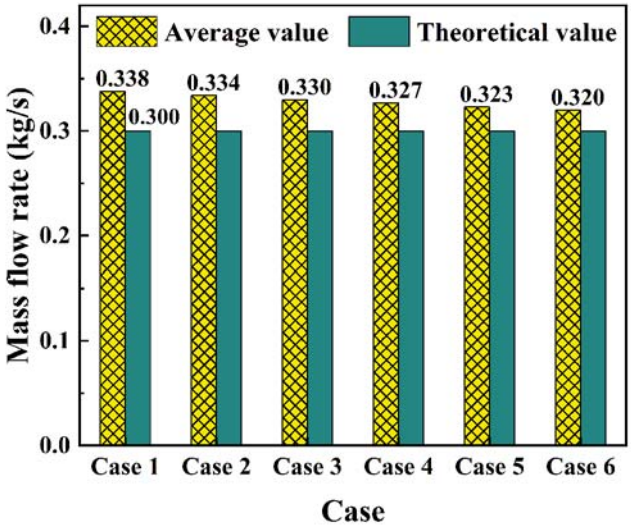

Figure 12. Comparison of the average value and theoretical value under different cases

stable stage. No matter at which stage, there are large fluctuations in the flow curve at low operating pressure conditions. The fluctuations decrease significantly as the operating pressure increases, especially in Case 6, where the curve appears to be very smooth and can maintain the stable output of powder for a long time. When the process of powder fluidization conveying is coming to an end, the instantaneous flow rates for the different cases start to decrease, and the moment corresponding to the decreasing inflection point is delayed with the increase of the operating pressure.

Figure 12 shows the average powder mass flow rate in the stable stage compared with the theoretical value calculated from Eq. (22). As can be seen, the average value shows a small difference in all cases, while the value in Case 1 is the largest, indicating that the maximum amount of powder is exported at this stage, and therefore, the powder mass flow rate drops sharply after t = 1.85 s. In addition, it can also be seen that the theoretical value calculated by Eq. (22) is lower than the average value in all cases, and the average error range of calculation accuracy is about 9.3%. Figure 13 shows the standard deviation of the powder mass flow rate distribution for all cases. It can be seen that the standard deviation decreases with the increase of operating pressure. Compared with the operating pressure of 0.5 MPa, the powder mass flow rate fluctuation under 3.0 MPa is reduced by 37.8%, indicating that the increase of operating pressure is beneficial to reduce the degree of powder mass flow rate fluctuation and improve the stability of powder fuel delivery. Analysis of comprehensive pressure and powder flow rate characteristics indicates that higher operating pressure can make the

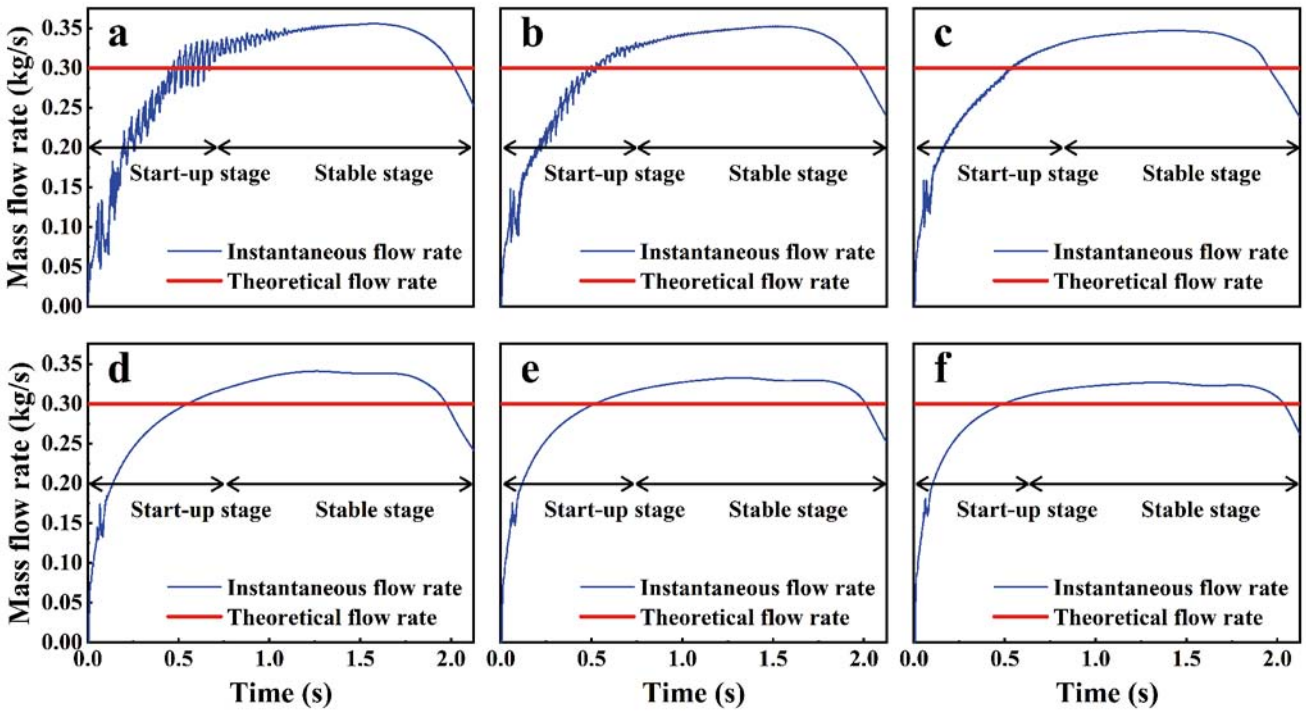

Figure 11. Powder mass flow rate distribution: (a) Case 1; (b) Case 2; (c) Case 3; (d) Case 4; (e) Case 5; (f) Case 6

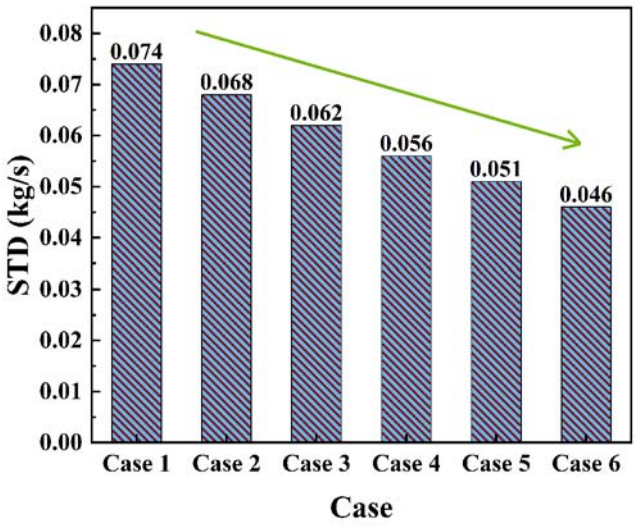

Figure 13. The standard deviation distribution of instantaneous mass flow rate under different cases

system maintain a relatively stable working condition, which is more conducive to maintaining the stability of powder fluidization and flow rate delivery.

CONCLUSION

In this work, the Eulerian-Eulerian TFM is chosen to describe the dense gas-solid two-phase flow for the piston-driving powder fuel supply system. The effect of operating pressure on the powder fluidization process and conveying characteristics is analyzed numerically. The main conclusions are as follows.

(1) The gas-solid pulsations at different operating pressures are mainly concentrated in the upper part of the powder storage tank, where eventually a stable gas-solid interface can be formed. As operating pressure increases, the powder layer area (ε_p = 0.1) and fluctuation amplitude decrease.

(2) As the operating pressure increases from 0.5 MPa to 3.0 MPa, the mean powder velocity in the range of Y-axial 0.012 m to 0.030 m decreases. When the operating pressure is 3.0 MPa, the rising time and fluctuation rate of pressure are reduced by 71.4% and 62.3%, respectively, and a long stable period exists for the pressure in the powder storage tank.

(3) In the stable conveying stage, the average powder mass flow rate increases with the increase of operating pressure, which is all higher than the theoretical value. The outlet powder mass flow rate fluctuation under high initial operating pressure is substantially decreased, which is more conducive to the stable conveying of powder.

NOMENCLATURE

Symbols

C_d – Drag coefficient
d_s – Powder diameter (mm)
e – Coefficient of restitution for solid collisions
$\mathbf{g}$ – Gravitational acceleration (m/s^2)
g_0 – Radial distribution function
λ_g – Gas bulk viscosity ($pa{\cdot}s$)
$\mathbf{I}$ – Stress tensor
I_{2D} – The second invariant of the deviatoric stress tensor
P – Pressure (N/m^2)
P_s – Solid pressure (N/m^2)
R_g – Gas constant [$J/(mol{\cdot}K)$]
T – Temperature (K)
t – Time (s)
$\mathbf{u}_g$ – Gas velocity (m/s)
$\mathbf{u}_s$ – Solid velocity (m/s)
Re_s – Reynolds number of the solid

Greek symbols

β – Gas-solid momentum exchange coefficient [$kg/(m^3s)$]
$\gamma_{\Theta s}$ – Collisional dissipation of energy [$kg/(m^3s)$]
ε_g – Gas volume fraction
ε_s – Solid volume fraction
$\varepsilon_{s,\,\max}$ – Maximum packing limit of solid
Θ_s – Granular temperature (m^2/s^2)
λ_s – Solid bulk viscosity ($pa{\cdot}s$)
μ_g – Gas shear viscosity ($pa{\cdot}s$)
μ_s – Solid effective viscosity ($pa{\cdot}s$)
$\mu_{s,\,col}$ – Solid collision viscosity ($pa{\cdot}s$)
$\mu_{s,\,fr}$ – Solid frictional viscosity ($pa{\cdot}s$)
$\mu_{s,\,kin}$ – Solid kinetic viscosity ($pa{\cdot}s$)
ϱ_g – Gas density (kg/m^3)
ϱ_s – Solid density (kg/m^3)
τ_g – Stress-strain tensor for gas phase (N/m^2)
τ_s – Stress-strain tensor for solid phase (N/m^2)
ϕ – Angle of internal friction (°)

ACKNOWLEDGEMENT

This research was supported by the National Natural Science Foundation of China (grant number: 12102161) and the Aeronautical Science Foundation of China (grant number: 20200001056001).

LITERATURE CITED

1. Du, Z., Huang, W. & Yan, L. (2020). Investigation on the supplementary combustion scheme for the divergent section of a solid rocket engine nozzle. *Energy* 190, 116295. DOI: 10.1016/j.energy.2019.116295.

2. Elfasakhany, A. (2021). Investigation of biomass powder as a direct solid biofuel in combustion engines: Modelling assessment and comparisons. *Ain. Shams. Eng. J.* 12 (3), 2991–2998. DOI: 10.1016/j.asej.2021.03.005.

3. Li, C., Hu, C., Xin, X., Li, Y. & Sun, H. (2016). Experimental study on the operation characteristics of aluminum powder fueled ramjet. *Acta Astronautica* 129, 74–81. DOI: 10.1016/j.actaastro.2016.08.032.

4. Li, W., Chen, X., Zhao, D., Wang, B., Ma, K. & Cai, T. (2020). Swirling effect on thermodynamic performance in a solid fueled ramjet with paraffin-polyethylene. *Aerosp. Sci. Technol*. 107, 106341. DOI: 10.1016/j.ast.2020.106341.

5. Li, Y., Hu, C., Deng, Z., Li, C., Sun, H. & Cai, Y. (2017). Experimental study on multiple-pulse performance characteristics of ammonium perchlorate/aluminum powder rocket motor. *Acta Astronautica* 133, 455–466. DOI: 10.1016/j.actaastro.2016.11.014.

6. Li, M., Hu, C., Wang, Z., Li,. Y., Hu, J., Hu, X. & Li, C. (2022). Application and performance estimation of Mg/CO_2 engine on Mars. *Acta Astronautica* 192, 314–327. DOI: 10.1016/j.actaastro.2021.12.032.

7. Wei, R., Hu, C., Wu, F., Hu, J., Zhu, X., Yang, J., Li, F. & Li, C. (2021). Heat-transfer characteristics of CO_2 boiling flow in the regenerative cooling channel of an Mg/CO_2 powder rocket engine for Mars missions. *Acta Astronautica* 189, 43–54. DOI: 10.1016/j.actaastro.2021.08.010.

8. Miller, T., Walter, J. & Kiely, D. (2002). A next-generation AUV energy system based on aluminum-seawater combustion. Workshop on Autonomous Underw. Vehicles 111–119. DOI: 10.1109/AUV.2002.1177213.

9. Yang, Y. & He, M. (2012). Numerical study on operating characteristics of a magnesium-based fuel ramjet. *Acta Astronautica* 79, 96–106. DOI: 10.1016/j.actaastro.2012.04.027.

10. Adnan, M., Sun, J., Ahmad, N. & Wei, J. (2021). Verification and validation of the DDPM-EMMS model for numerical simulations of bubbling, turbulent and circulating fluidized beds. *Powder Technol*. 379, 69–88. DOI: 10.1016/j.powtec.2020.10.041.

11. Chen, M., Chen, Z., Gong, M., Tang, Y. & Liu, M. (2021). CFD–DEM–VDGM method for simulation of particle fluidization behavior in multi-ring inclined-hole spouted fluidized bed. *Particuology* 57, 112–126. DOI: 10.1016/j.partic.2021.01.004.

12. Fricke, H. & Sobieniak, M. (1970). Fluidized Powders—A New Approach to Storable Missile Fuels[C]. Denver: 12th JANNAF Liquid Propulsion Meeting.

13. Meyer, M. (1993). Powdered aluminum and oxygen rocket propellants: Subscale combustion experiments. NASA-TM-1993-106439.

14. Foote, J. & Litchford, R. (2005). "Powdered Magnesium: Carbon Dioxide Combustion for Mars Propulsion". AIAA-2005-4469. DOI: 10.2514/6.2005-4469.

15. Miller, T. & Herr, J. (2004). Green Rocket Propulsion by Reaction of Al and Mg Powders and Water. 40th AIAA/ASME/SAE/ASEE Joint Propulsion Conference and Exhibit. DOI: 10.2514/6.2004-4037.

16. Cai, L., Liu, S., Pan, X., Xu, G., Chen, X. & Zhao, C. (2014). Influence of carbonaceous powders on flow characteristics of dense-phase pneumatic conveying at high pressure. *Exp. Therm. Fluid Sci*. 58 (4), 121–130. DOI: 10.1016/j.expthermflusci.2014.06.020.

17. Song, J., Liu, D., Ma, J. & Chen, X. (2018). Effect of elevated pressure on bubble properties in a two-dimensional gas–solid fluidized bed. *Chem. Eng. Res. Des*. 138, 21–31. DOI: 10.1016/j.cherd.2018.08.012.

18. Liu, D., Hu, J., Song, J., Liang, C. & Chen, X. (2020). Effect of elevated pressure on gas-solid flow characteristics in a circulating fluidized bed. *Powder Technol*. 366, 470–476. DOI: 10.1016/j.powtec.2020.02.046.

19. Shabanian, J. & Chaouki, J. (2016). Effects of temperature, pressure, and interparticle forces on the hydrodynamics of a gas-solid fluidized bed. *Chem. Eng. J*. 313, 580–590. DOI: 10.1016/j.cej.2016.12.061.

20. Sun, H., Hu, C. & Zhu, X. (2017). Numerical simulation on the powder propellant pickup character-istics of feeding system at high pressure. *Acta Astronautica* 139 (10), 85–97. DOI: 10.10164/j.actaastro.2017.06.030.

21. Sun, H., Hu, C., Zhang, T. & Deng, Z. (2016). Experimental investigation on mass flow rate measurements and feeding characteristics of powder at high pressure. *Appl. Therm. Eng*. 102, 30–37. DOI: 10.1016/j.applthermaleng.2016.03.142.

22. Shao, Y., Li, Z., Zhong, W., Bian, Z. & Yu, A. (2020). Minimum fluidization velocity of particles with different size distributions at elevated pressures and temperatures. *Chem. Eng. Sci*. 216. 115555. DOI: 10.1016/j.ces.2020.115555.

23. Yang, J., Hu, C., Qiang, W., Hu, J., Hu, X. & Zhu, X. (2021). Experimental investigation on the starting and flow regulation characteristics of powder supply system for powder engines. *Acta Astronautica* 180, 73–84. DOI: 10.1016/j.actaastro.2020.12.004.

24. Kuipers, J., Van, Duin, K., Van, Beckum, F. & Van, Swaaij, W. (1992). A numerical model of gas-fluidized beds. *Chem. Eng. Sci*. 47 (8), 1913–1924. DOI: 10.1016/0009-2509(92)80309-Z.

25. Gidaspow, D. (1994). Multiphase flow and fluidization: Continuum and kinetic theory descriptions, published by Academic Press. San Diego. 83 (3), 287. DOI: 10.1016/0032-5910(95)90055-1.

26. Plewik, R., Synowiec, P. & Wójcik, J. (2008). Two-phase CFD simulation of the monodyspersed suspension hydraulic behaviour in the tank apparatus from a circulatory pipe. *Polish J. Chem. Technol*. 10 (1), 22–27. DOI: 10.2478/v10026-008-0006-6.

27. Zhu, X., Dong, P., Tu, Q., Zhu, Z., Yang, W. & Wang, H. (2020). Investigation of gas-solids flow characteristics in a pressurised circulating fluidised bed by experiment and simulation. *Powder Tech*nol. 366, 420–433. DOI: 10.1016/j.powtec.2020.02.047.

28. Alder, B. & Wainwright, T. (1960). Studies in Molecular Dynamics. II. Behavior of a Small Number of Elastic Spheres. *J. Chem. Phys*. 33 (5). 1349–1451. DOI: 10.1063/1.1731425.

29. Gidaspow, J. (1990). A bubbling fluidization model using kinetic theory of granular flow. *AIChE. J.* 36 (4), 523–538. DOI: 10.1002/aic.690360404.

30. Nieuwland, J., Sint,, A., Kuipers, J. & Wpm, S. (1996). Hydrodynamic modelling of gas-particle flows in riser reactors. *AlChE. J.* 42 (6). DOI: 10.1002/aic.690420608.

31. Huilin, L., Gidaspow, D., Bouillard, J. & Wentie, L. (2003). Hydrodynamic simulation of gas–solid flow in a riser using kinetic theory of granular flow. *Chem. Eng. J.* 95 (1), 1–13. DOI: 10.1016/S1385-8947(03)00062-7.

32. Du, W., Bao, X., Xu, J. & Wei, W. (2006). Computational fluid dynamics (CFD) modeling of spouted bed: Assessment of drag coefficient correlations. *Chem. Eng. Sci.* 61 (5), 1401–1420. DOI: 10.1016/j.ces.2005.08.013.

33. Panneerselvam, R., Savithri, S. & Surender, G. (2007). CFD based investigations on hydrodynamics and energy dissipation due to solid motion in liquid fluidised bed. *Chem. Eng. J.* 132 (1), 159–171. DOI: 10.1016/j.cej.2007.01.042.

34. Behjat, Y., Shahhosseini, S. & Hashemabadi, S. (2008). CFD modeling of hydrodynamic and heat transfer in fluidized bed reactors. Int. Commun. *Heat Mass Transf*. 35 (3), 357–368. DOI: 10.1016/j.icheatmasstransfer.2007.09.011.

35. Jie, L. & Kuipers, J. (2002). Effect of pressure on gas–solid flow behavior in dense gas-fluidized beds: a discrete particle simulation study. *Powder Technol.* 127 (2), 173–184. DOI: 10.1016/S0032-5910(02)00116-X.

36. Rongtao, F., Junguo, L., Libo, D., Zhenhua, H., Zhongren, B., Haijuan, Z. & Yitian, F. (2018). Gas-solid flow behaviors in a multi-stage circulating fluidized bed under elevated pressure. *Chem. Eng. Sci.* 196, 1–13. DOI: 10.1016/j.ces.2018.11.057.